# Rupture Segmentation of the 14 August 2021 $M_{\rm w}$ 7.2 Nippes, Haiti, Earthquake Using Aftershock Relocation from a Local Seismic Deployment

Roby Douilly<sup>\*1</sup>, Sylvert Paul<sup>2,3,4</sup>, Tony Monfret<sup>2,4,5</sup>, Anne Deschamps<sup>2,4</sup>, David Ambrois<sup>2,4</sup>, Steeve J. Symithe<sup>3,4</sup>, Sadrac St Fleur<sup>3</sup>, Françoise Courboulex<sup>2,4</sup>, Eric Calais<sup>2,4,6</sup>, Dominique Boisson<sup>3,4</sup>, Bernard Mercier de Lépinay<sup>2,4</sup>, Yvonne Font<sup>2,4</sup>, and Jérôme Chèze<sup>2,4</sup>

#### - ABSTRACT -

The 14 August 2021  $M_{\rm w}$  7.2 Haiti earthquake struck 11 yr after the devastating 2010 event within the Enriquillo Plantain Garden (EPG) fault zone in the Southern peninsula of Haiti. Space geodetic results show that the rupture is composed of both left-lateral strike-slip and thrust motion, similar to the 2010 rupture; but aftershock locations from a local short-period network are too diffuse to precisely delineate the segments that participated in this rupture. A few days after the mainshocks, we installed 12 broadband stations in the epicentral area. Here, we use data from those stations in combination with four local Raspberry Shakes stations that were already in place as part of a citizen seismology experiment to precisely relocate 2528 aftershocks from August to December 2021, and derive 1D P- and S-crustal velocity models for this region. We show that the aftershocks delineate three north-dipping structures with different strikes, located to the north of the EPG fault. In addition, two smaller aftershock clusters occurred on the EPG fault near the hypocenter area, indicative of triggered seismicity. Focal mechanisms are in agreement with coseismic slip inversion from Interferometric Synthetic Aperture Radar data with nodal planes that are consistent with the transpressional structures illustrated by the aftershock zones.

#### **KEY POINTS**

- Aftershocks are used to delineate the geometry of the faults that ruptured during the M<sub>w</sub> 7.2 Haiti earthquake.
- Aftershocks delineated three clusters with slightly variable dip.
- First-motion focal mechanisms are primarily composed of both left lateral strike-slip and thrust motions.

**Supplemental Material** 

# **INTRODUCTION**

The 14 August 2021  $M_{\rm w}$  7.2 Nippes, Haiti, earthquake is the second major event to strike southern Haiti this century, 11 yr after the devastating 2010  $M_{\rm w}$  7.0 event. These two earthquakes struck a fault zone that encompasses the Enriquillo Plantain Garden (EPG) fault that cuts through the southern peninsula of Haiti in the east–west direction and accommodates part of the relative motion between the Caribbean and North American plates. Geological mapping shows that the EPG fault is a left-lateral strike-slip fault with geomorphic evidence for

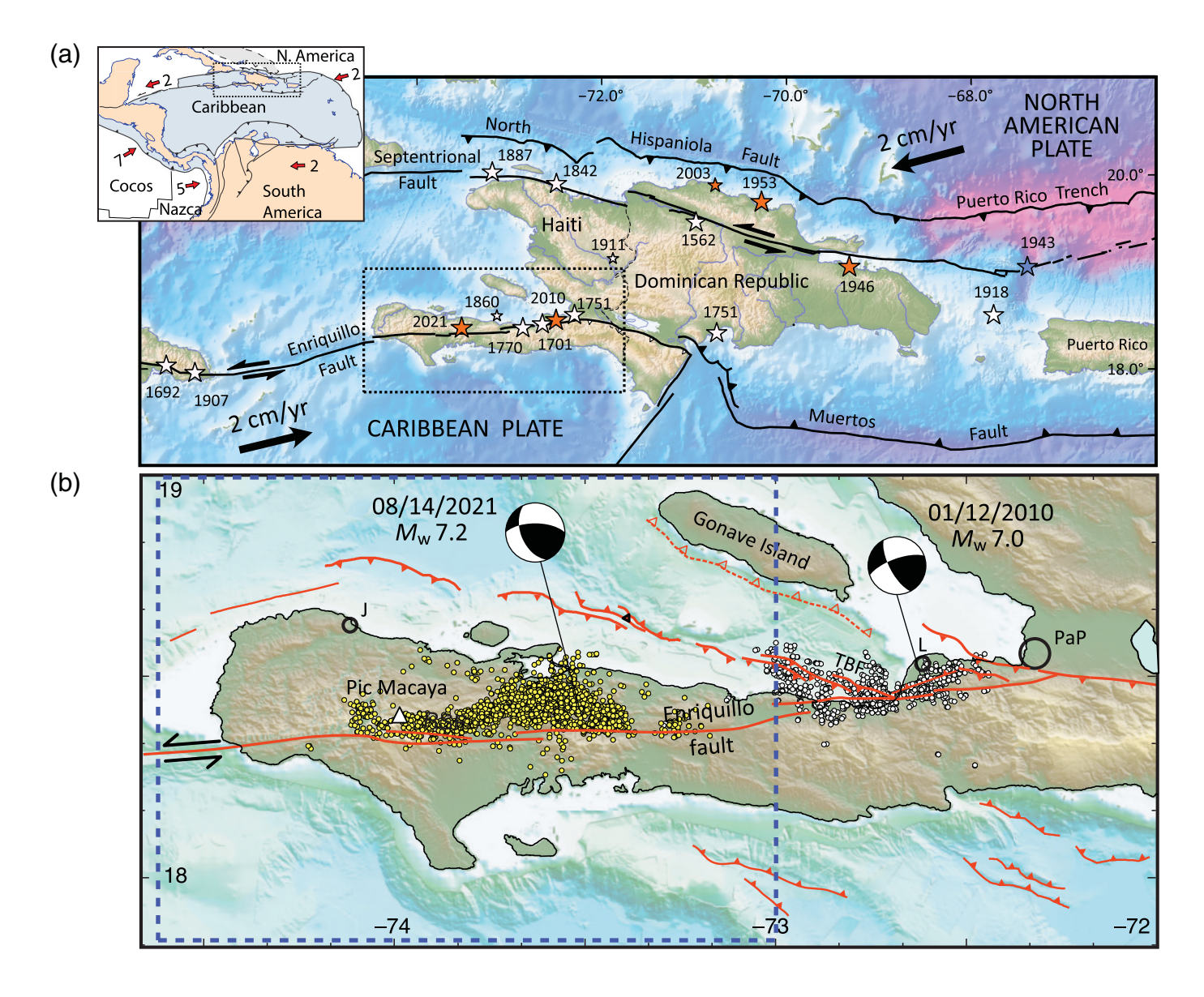
Quaternary activity (Mann *et al.*, 1995; Saint Fleur *et al.*, 2015) and a geodetically determined slip rate of 7–9 mm/yr (Benford *et al.*, 2012; Symithe *et al.*, 2015). Historical archives show that southern Haiti was struck by four significant earthquakes in the

1. Department of Earth and Planetary Sciences, University of California, Riverside, Riverside California, U.S.A., https://orcid.org/0000-0003-1724-2535 (RD);
2. Université Côte d'Azur, CNRS, IRD, Observatoire de la Côte d'Azur, Géoazur, France, https://orcid.org/0000-0003-4132-7635 (SP); https://orcid.org/0000-0002-4521-0357 (TM); https://orcid.org/0000-0002-6209-9814 (AD); https://orcid.org/0000-0002-4467-9102 (FC); https://orcid.org/0000-0002-5935-8117 (EC); https://orcid.org/0000-0002-9804-943X (BMdL); https://orcid.org/0000-0002-9553-5280 (YF); https://orcid.org/0000-0002-7644-3989 (JC); 3. Faculté des Sciences, Unité de Recherche en Géosciences (URGeo), Port-au-Prince, Haiti; https://orcid.org/0000-0003-1133-202X (SJS); https://orcid.org/0000-0002-7136-7235 (DB); 4. CARIBACT Joint Research Laboratory, Port-au-Prince, Haiti; 5. Barcelona Center for Subsurface Imaging, Institut de Ciències del Mar (ICM), CSIC, Barcelona, Spain; 6. Department of Geosciences, Ecole Normale Supérieure, Paris, France

\*Corresponding author: robyd@ucr.edu

**Cite this article as** Douilly, R., S. Paul, T. Monfret, A. Deschamps, D. Ambrois, S. J. Symithe, S. St Fleur, F. Courboulex, E. Calais, D. Boisson, *et al.* (2022). Rupture Segmentation of the 14 August 2021  $M_{\rm w}$  7.2 Nippes, Haiti, Earthquake Using Aftershock Relocation from a Local Seismic Deployment, *Bull. Seismol. Soc. Am.* **113**, 58–72, doi: 10.1785/0120220128

© Seismological Society of America



eighteenth century in 1701, 1751, 1751, and 1770 and a sequence of moderate earthquakes in 1860 (Scherer, 1912; Vogt, 2004, 2005; Bakun *et al.*, 2012), followed by a long period of relative quiescence until 2010. To the north, the remainder of the relative motion between the Caribbean and North American plates is taken up by the Oriente–Septentrional strike-slip fault and, further north, by the North Hispaniola thrust fault, continuous to the east with the Puerto Rico trench (Fig. 1).

The 2010 earthquake occurred near Léogâne with an epicenter less than 25 km from the capital city of Port-au-Prince (Nettles and Hjörleifsdóttir, 2010). The rupture was initially believed to have initiated on the EPG fault, on the basis of the proximity of the mainshock epicenter to that fault. Most subsequent finite-fault inversions using geodetic (Interferometric Synthetic Aperture Radar [InSAR] and Global Positioning System [GPS]), seismological (teleseismic data), and geological data (coral uplift) concluded that more than 80% of the seismic moment was released on a north-dipping fault, different from the EPG fault, referred to as the Léogâne fault (Calais et al., 2010;

Figure 1. (a) Seismotectonic context of the Caribbean-North American plate boundary at the longitude of Hispaniola. Main active faults are shown with black lines. Stars indicate major destructive historical (white) and instrumental (red) earthquakes (Scherer, 1912; Bakun et al., 2012). Large arrows show the relative motion between the Caribbean and North American plates. The black dashed rectangle displays the area shown in (b). Top left inset shows the large-scale tectonic setting of the study area, with arrows showing the Global Positioning System (GPS)-derived velocity of the surrounding plates with respect to the Caribbean. Numbers are in centimeters per year. (b) Active faults with red lines from E. Calais, S. J. Symithe, and B. M. de Lépinay (unpublished manuscript, 2022, see Data and Resources) in the southern peninsula of Haiti. The white circles mark the aftershock distribution for the 2010 Haiti earthquake (Douilly et al., 2013), and the yellow circles indicate the aftershock relocation for the 2021 Nippes rupture from this study. The blue dashed rectangle shows the area encompassed in Figure 6 and beyond. J, Jérémie; L, Léogâne; PaP, Port-au-Prince; and TBF, Trois Baies fault.

Hayes et al., 2010). The 2010 earthquake ruptured at least two fault segments: A first one in the east with mostly reverse motion, and then propagated westward to a second, strike-slip,

segment but did not transfer to the nearby EPG fault (Douilly et al., 2013; Symithe et al., 2013). Dynamic rupture models show that the two ruptures are well explained by the successive rupture of two fault segments oriented favorably with respect to the rupture propagation, whereas the geometry of the EPG fault did not allow shear stress to reach failure (Douilly et al., 2015).

Although a detailed analysis of the 2010 earthquake aftershocks, hence a direct characterization of the rupture geometry, had to wait for the analysis of data from the deployment of a temporary seismic network (Douilly et al., 2013), a rapid preliminary analysis of the 2021 earthquake was made possible; thanks to low-cost, citizen-hosted seismic stations that operated during and after the mainshock (Calais et al., 2022). Their realtime data allowed for the rapid identification of two aftershock clusters that coincide with the two areas of coseismic slip identified in inversions of conventional seismological and geodetic data. The 2021 rupture bears similarities with its 2010 counterpart, as the event is transpressional, initiated on a mostly reverse fault segment, and then propagated westward onto a purely strike-slip segment. Though the presence of citizen-hosted seismic stations proved invaluable for a rapid assessment of the 2021 earthquake source, much remains to be understood, as the low-cost stations used in this preliminary analysis have a limited dynamic range (Anthony et al., 2019) and are sparsely distributed. A rapid field response led by the Haiti State University in collaboration with other institutions from France and United States, however, allowed for the deployment of 12 broadband seismic stations in the epicentral area within 6-10 days of the mainshock.

Ground deformation from InSAR interferogram images indicates that the eastern half of the rupture is dominated by reverse motion, whereas the western half has mostly left-lateral motion, with coseismic ground displacement limited to the north of the EPG fault (Calais et al., 2022; Maurer et al., 2022). This implies that the 2021 rupture occurred on a secondary unmapped fault, as in 2010, or that it ruptured the EPG fault proper, but with a curved geometry at depth. To test these possibilities, and considering that well-located early aftershocks tend to better delineate the ruptured segments that participated in the mainshock (Ratchkovski et al., 2004; Douilly et al., 2013; Shelly, 2020), we used a subset of the aftershocks detected from August to December 2021 to infer a 1D P- and S-crustal velocity model for this region and to precisely relocate those aftershocks to resolve the geometry of the fault segments involved in the rupture.

# **DATA AND METHODS**Station deployment

A few days following the 14 August 2021 mainshock, we deployed 10 Nanometric and two Güralp broadband seismic stations in the epicentral area to complement the four local four-component (three-component accelerometer and one-component velocimeter) Raspberry Shake (RS) stations that

were installed during the citizen seismology experiment in southwestern Haiti (Calais et al., 2022). The real-time aftershock detection from the ayiti-séisme platform allowed us to optimize the geographic distribution of broadband stations. Each Nanometric station consists of a Trillium Compact 120 s posthole broadband seismometer—a 24-bit Centaur digital recorder and the remaining accessories such as GPS receiver, 12V battery, solar panels, and a deployment box. The Güralp systems, installed three days after the earthquake, were each composed of a 24-bit Minimus recorder associated with CMG40T broadband sensor and other accessories such as a GPS receiver, a 12V battery, and a solar panel. All the stations were fully operational starting 25 August 2021, and we plan on leaving them in the field for at least a year to continuously record the seismic data. The first service maintenance and data collection took place in early October 2021, but two stations had stopped working. Station PEST had a battery problem that was later fixed. The solar panel at station LBOR was stolen, so we decided to move it to a more secure location and rename it SALO. This renamed station was operational on 10 October. The complete list of all broadband and short-period RS stations with their deployment date is given in Table 1.

## Event detection and magnitude calculation

In this study, we used continuous waveforms recorded between 20 August and 31 December 2021. In total, 63 GB of recordings were collected by the temporary stations over the studied period. The waveforms were stored in standard miniSEED format in a database organized by daily continuous files (24 hr), completed with data from the four RS of the HY Haiti network. Such a database allows for direct access to the data with the processing software and for verifying data availability via the International Federation of Digital Seismograph Networks (FDSN) webservice. We use SeisComp3 (SC3)—a tool for real-time monitoring—to analyze the data. The real-time stream is simulated with records collected by injecting time-ordered multiplexed data (playback) in blocks of 24 hr.

The data are processed in two steps. The first one is a phase detection based on a standard short-term average/long-term average (STA/LTA) analysis (0.5-60 s) (Allen, 1982) on filtered data (4-20 Hz). These parameters have been defined in such a way that the algorithm is sensitive to rapid increases in amplitude over time, characteristic of local earthquakes. For S phases, we use the Akaike Information Criterion (AIC) (Maeda, 1985) detection algorithm implemented in SC3. The second step is the association of the automatic picks. This is performed by the SC3 scanloc module, which uses Density-Based Spatial Clustering of Applications with Noise (Ester et al., 1996)—a machine learning algorithm for clustering tasks. To limit false detections, the minimum of six associated phases is required to create an event. In total, the automatic catalog contains 5560 events detected and located during the time interval considered here. We calculate the

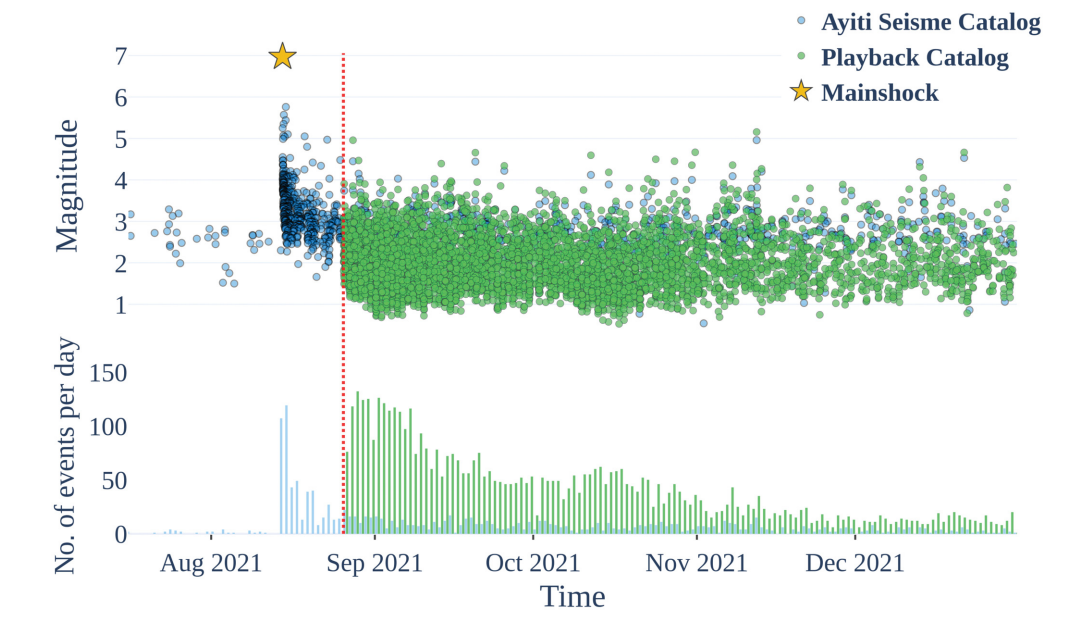


**Figure 2.** Temporal variation of seismicity from the ayiti séisme catalog (real-time detection in blue) and the playback catalog (green) with temporary stations. The top panel is the distribution with respect to magnitude, and the bottom panel is the distribution with respect to the number of events per day. The yellow star marks the mainshock, and the red dashed line indicates the installation date of the temporary stations. More significant daily events are detected with the temporary stations.

magnitude of these events and compare the event detection from the playback catalog with the ayiti-séisme catalog (Fig. 2). With the addition of the local broadband stations, we were able to detect significantly more daily events and with lower magnitude compared to the original catalog.

# Velocity and hypocenter determination

To properly delimitate the structures involved in 2021 earthquake, we selected a subset of well-located aftershocks within the original catalog described earlier. decided to only use local stations in our analysis, since a 1D velocity model would not be able to fully accommodate the phase delays from the distant regional stations considering the heterogeneity of the crustal structure over the Hispaniola island (Douilly et al., 2016; Corbeau et al., 2017; Quiros et al., 2018; Possee et al., 2019). We retain a total of 2877 aftershocks with 22,249 P-wave arrivals and 9652 S-wave arrivals that have a root mean square (rms < 0.7 s) and that are only located on land and inside the area covered by our stations.

Therefore, all the events that occurred offshore near the town of Jérémie or near the 2010 rupture by Léogâne are not considered in the analysis subsequently. We then used the location software Velest (Kissling *et al.*, 1994, 1995) to jointly invert those arrivals for the 1D *P*- and *S*-velocity models, hypocenter

TABLE 1

Station Information with Their P- and S-Time Corrections Obtained from the Joint Inversion

Name	Code	Longitude (°)	Latitude (°)	Elevation (m)	P-Wave Station Correction (s)	S-Wave Station Correction (s)	Date Installed (yyyy/mm/dd)	Date Recovered (yyyy/mm/dd)	Station Type
CHARD	Z2	-74.166	18.275	8	0.38	0.39	2021/08/27	_	Nanometrics
HBAR	Z2	-73.643	18.481	19.2	-0.08	-0.41	2021/08/18	_	Güralp
PBEAU	Z2	-73.957	18.477	600	0.11	-0.24	2021/08/26	_	Nanometrics
CAMPP	Z2	-73.386	18.325	215	0.15	-0.12	2021/08/26	_	Nanometrics
SALO	Z2	-73.616	18.227	0	0.12	-0.15	2021/10/02	_	Nanometrics
CAVA	Z2	-73.656	18.415	784	0.06	-0.19	2021/08/26	_	Nanometrics
BFIN	Z2	-73.612	18.394	454	0.00	-0.29	2021/08/17	_	Nanometrics
HASL	Z2	-73.415	18.384	157	0.46	0.72	2021/08/17	_	Güralp
ROCH	Z2	-73.016	18.180	24	0.09	-0.23	2021/08/26	_	Nanometrics
STTHE	Z2	-73.993	18.534	204	0.21	-0.10	2021/08/26	_	Nanometrics
LBOR	Z2	-73.804	18.280	66	0.23	0.03	2021/08/27	2021/09/21	Nanometrics
TROU	Z2	-73.474	18.513	31	0.17	0.04	2021/08/25	_	Nanometrics
PEST	Z2	-73.799	18.541	39	0.01	-0.41	2021/08/25	_	Nanometrics
SPRIV	HY	-73.244	18.477	1	0.93	0.00	2021/08/18	_	Raspberry Shake
SAQUI	HY	-73.397	18.283	26	0.11	0.00	2021/08/18	_	Raspberry Shake
SMESL	HY	-73.616	18.227	0	0.17	0.00	2020/12/10	_	Raspberry Shake
SJER2	HY	-74.121	18.650	19	0.51	0.00	2019/09/10	_	Raspberry Shake

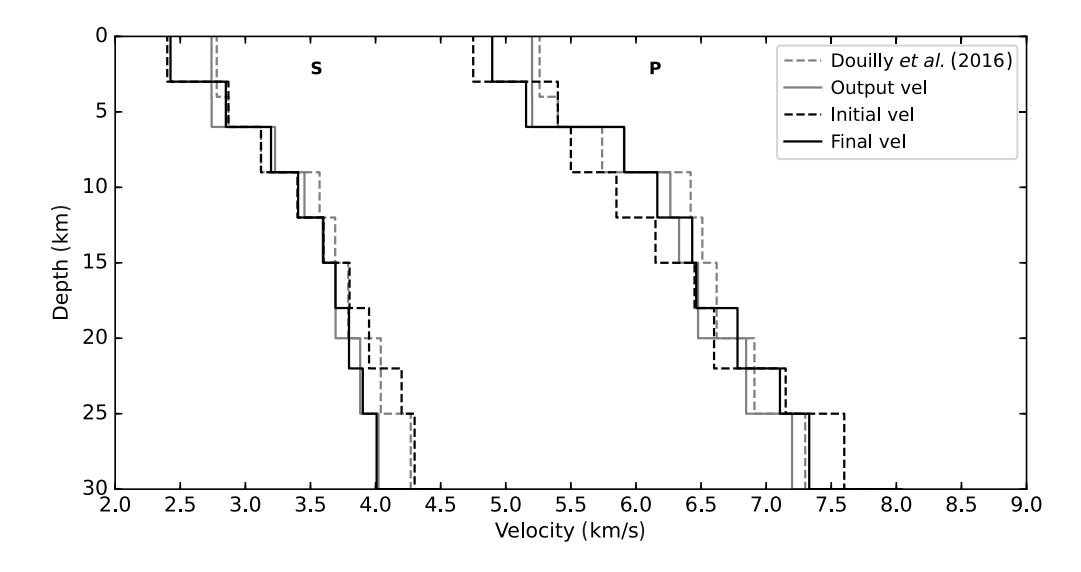


**Figure 3.** One-dimensional *P*- and *S*-velocity profiles considering two input velocities. Initial models are shown with dashed lines, and final models after several runs are shown with solid lines.

locations, and station corrections. After performing the jointhypocenter inversion, we incorporated the final velocity model and hypocenter locations from Velest into the hypoDD doubledifference software (Waldhauser and Ellsworth, 2000, 2002; Waldhauser, 2001) to reduce the first-order scattering effect due to regional heterogeneities and to further improve the aftershock locations. The double-difference method iteratively minimizes the residual between the observed and calculated travel times for pairs of earthquakes observed at common stations by changing their hypocenter vector. This approach cancels common errors when the distribution of seismicity is sufficiently dense and can better delineate the active structures. As an example, for the 2010 Haiti earthquake, the relocations from hypoDD were more tightly clustered compared to the Velest locations, and the ruptured segments were better defined (Douilly et al., 2013). However, the hypoDD earthquake catalog will have fewer events compared to the Velest catalog. This is due to the fact that by fixing the maximum event separation to 10 km and the number of links to define a neighbor to six, the reweighting process after each iteration will cause some events to exceed the separation criteria and be removed in the process (Waldhauser, 2001). Thus, after computing the inversion with hypoDD, the number of aftershocks is reduced to 2528 events, and those high-precision location events are then used to identify the structures that were activated by the mainshock.

## P-wave first-motion focal mechanisms

To investigate the deformation patterns of the ruptured segments delineated by the aftershock relocations, we manually picked 200 events from the hypoDD catalog with at least 10 *P*-wave first-motion polarities to compute their preferred fault-plane solution using the HASH software (Hardebeck and Shearer, 2008). Given the limited number of local stations

in our study, we also incorporate the manual picks from regional stations with the purpose of increasing the station distribution ratio and reducing the misfit to obtain a reliable set of focal mechanisms. We use the 1D velocity model obtained from the Velest joint inversion to compute take-off angles and determine the best focal mechanisms. Following Hardebeck Shearer (2008), we only consider focal mechanisms with a misfit less than 0.3 and a station distribution ratio greater than 0.3. This results in a focal mechanism dataset of 53 events.

#### **RESULTS**

# Minimum 1D velocity structure and station corrections

To derive the best-fitting velocity structure, we first select a subset of events that have the most recordings and an azimuthal gap less than 180°. We chose station BFIN as the reference (i.e., P station correction is set to zero), because it is located near the center of the aftershock zone and has the most recordings. We tested a range of starting velocity models including the recent one from Douilly et al. (2016) that was derived in the southeastern part of the peninsula near the 2010 mainshock. After several iterations, the residuals and average rms decrease from 0.40 and 0.16 s to 0.22 and 0.05 s, respectively. Figure 3 shows the results considering only two input velocity models (dashed lines). The velocities after the iterations are shown with solid lines, in which the black solid line is the final model used in this study. Despite the differences with the input velocities, the final models are consistent with each other, implying a good stability of our velocity models. We observe that the final P and S velocities for almost all the layers are consistently smaller compared to ones obtained further east near Léogâne by Douilly et al. (2016) (dashed gray lines in Fig. 3). In the upper 5 km, the decrease in velocity is on the order of 0.4 km/s for the *P* and  $\sim 0.1 \text{ km}$  for the *S*. For the layers between 8 and 18 km, the decrease is  $\sim$ 0.2 km/s for both *P* and *S*. This suggests that there is a lateral heterogeneity for both P and S velocities in the Southern Peninsula.

To further assess the sensitivity of the inversion to the initial parameters, we performed two additional tests. For the first test, we split the dataset equally into two groups with similar spatial distribution of aftershocks. Using the same initial model shown in dashed black line in Figure 3, we inverted both the groups individually and compared their final velocities. Figure 4

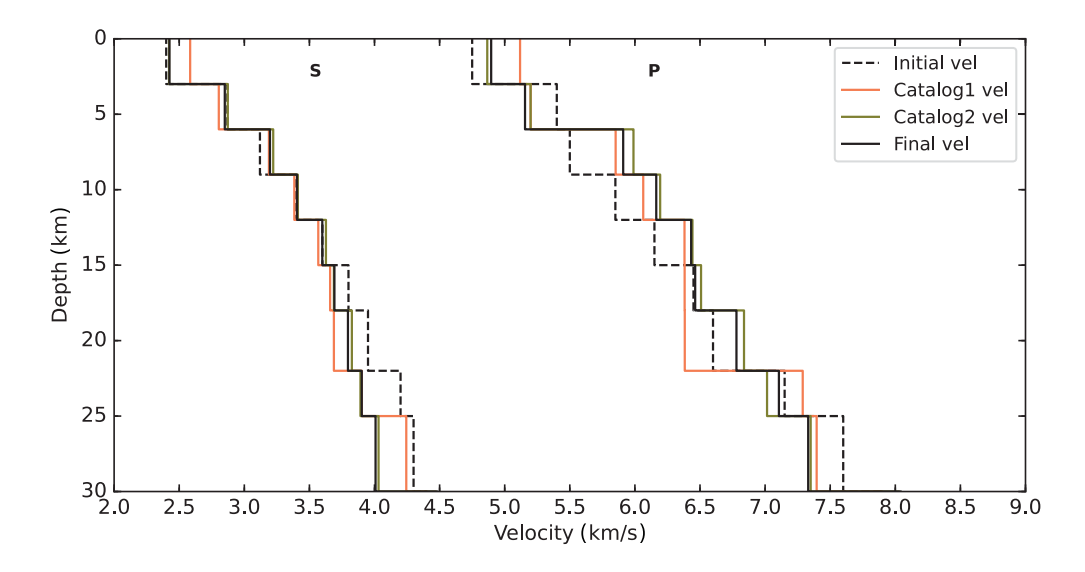


**Figure 4.** One-dimensional *P*- and *S*-velocity models for the two separate datasets. Initial models are shown with dashed lines, and final models after several runs are shown with solid lines.

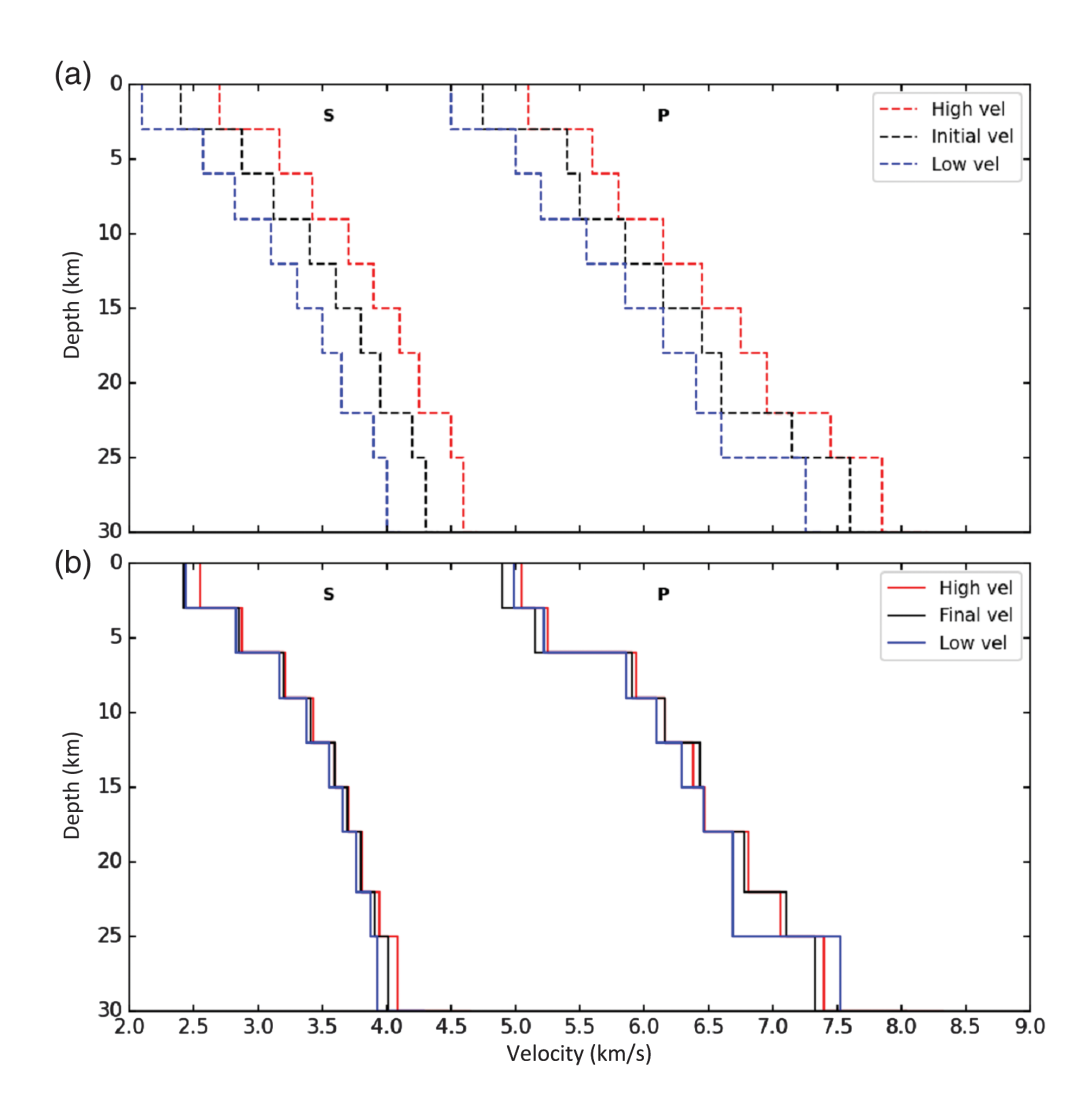


**Figure 5.** (a) One-dimensional velocity profiles for three different starting models in dashed lines. (b) Final velocity models (solid lines) for each model in (a). The black dashed line is the same starting velocity as in Figures 3 and 4.

compares the final velocity model from Figure 3 to the velocities for the two separate datasets. The velocities for the two datasets appear to converge toward our final velocity model for this region. Finally, similarly to Douilly et al. (2016), we used different starting model magnitudes with low and high values for the P and S models (dashed lines in Fig. 5). After inverting each of them, we observe that all models are converging to the final velocity model (solid lines in Fig. 5 and Table 2) that we will refer to as the minimum 1D velocity model for this region. Those two tests show high convergence and stability of our minimum 1D velocity model.

Using Velest, we also invert for the P and S station corrections, which are the average time residuals that the 1D velocity model could not fully accommodate due to a number of factors such as lateral heterogeneity of the velocity structure. The corrections are initially set to zero and vary during the inversion with respect to the reference station. Table 1 and Figure 6 show the final P and S station corrections. Considering that RS stations SPRIV, SJER2, SAQUI, and SMESL have only one vertical velocity component and no horizontal velocity components, their S station corrections are by default set to zero and should not be interpreted. RS stations SPRIV and SJRE2 have approximately eight times fewer P arrivals compared to the other two RS stations (SAQUI and SMESL), and thus their P station corrections are not well constrained. For the P-wave station correction distribution, we observe

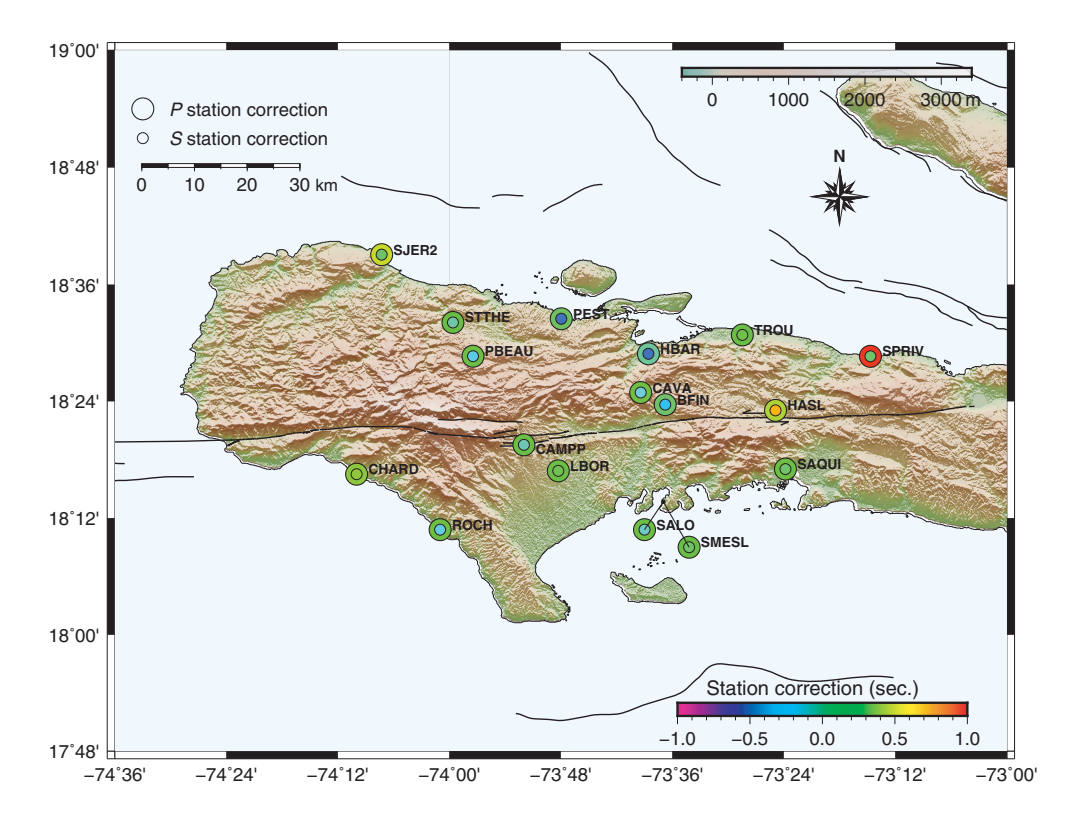


**Figure 6.** Spatial distribution of *P* and *S* station corrections for the local stations in southern Haiti. The outer circles mark the *P*-wave station corrections, and the inner circles mark the *S*-waves station corrections.

that the outermost stations (TROU, HASL, LBOR, and CHAR) have positive station corrections on the order of +0.2 to +0.3 s, whereas stations in the center of the network have either nearly zero (e.g., CAVA, PEST) or negative anomalies (e.g., HBAR). Stations SMESL and SALO are located on the same site, and as expected their *P* corrections are nearly the same, which further showcases the high accuracy and stability of the results. The *S*-wave station corrections show similar distribution as for the *P* corrections, for which stations TROU, HASL, LBOR, and CHAR have positive corrections, whereas the center stations

TABLE 2 **Best-Fitting 1D Model for the** *P***- and** *S***-Wave Velocity Structure** 

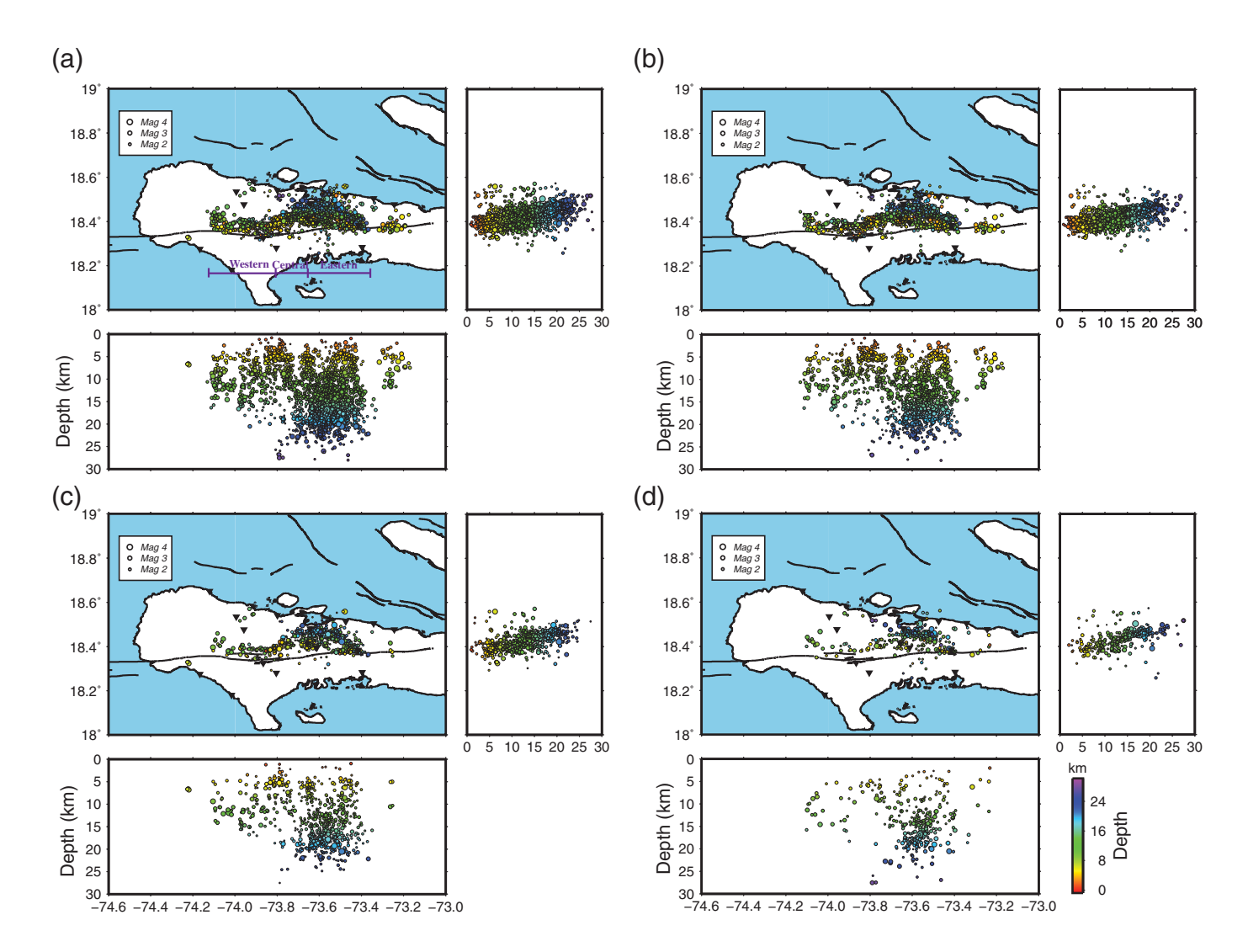
Depth (km)	V <sub>P</sub> (km/s)	V <sub>s</sub> (km/s)	$V_P/V_S$
0	4.90	2.42	2.02
3	5.16	2.85	1.81
6	5.91	3.20	1.85
9	6.16	3.41	1.81
12	6.43	3.60	1.79
15	6.46	3.69	1.75
18	6.78	3.80	1.78
22	7.11	3.90	1.82
25	7.33	4.01	1.83
30	8.04	4.49	1.79

such as PEST, HBAR, CAVA, and PBEA have negative corrections. This variability in station correction distribution is most likely due to a change in velocities, which further supports the argument of a lateral heterogeneity of the velocity model in the Southern Peninsula.

# Spatial distribution of aftershocks

After identifying the best-fit-1D velocity model (Table 2) from the joint inversion described earlier, we run the Velest program one last time to relocate the entire set of 2820 aftershocks by keeping the final P and S velocities and station corrections fixed. While doing so, we incorporate the hypocenter locations from Velest to hypoDD to further refine the locations using the catalog of phase arrival

picks only. For the reasons explained earlier, the hypoDD catalog is reduced to 2528 total events, and their locations, coded by hypocenter depth and magnitude, are shown in Figure 7a (see Table S1, available in the supplemental material to this article, for a complete list of the earthquake locations). Similar to the results of Calais et al. (2022), the aftershocks cluster north of the EPG fault has a spatial distribution that seems to follow the topography. Overall, the aftershock distribution illustrates several zones, or clusters, with slightly different behavior and orientation. The eastern one, which is located between the longitudes of -73.35° and -73.65°, shows a northwest-southeast-striking feature that has significantly more events compared to the other two clusters. Furthermore, events in this zone reach greater depth (up to ~25 km), whereas events in the other zones are shallower (the maximum depth ~15 km). In the center zone (from longitudes -73.65° to -73.8°), we observe a slight rotation in the strike of the aftershock cluster to a southwest-northeast strike with shallower events. As one moves west, aftershocks transition to an eastwest direction (longitudes -73.8° and -74.10°), which is in agreement with the orientation and surface trace of the Ravine du Sud fault (Saint Fleur et al., 2020). To better understand the vertical distribution of aftershocks, we represent them along different depth slices of ±2 km (Fig. 8). The structures described earlier are well expressed at different depth slices where the eastern, central, and western zones dip to the north



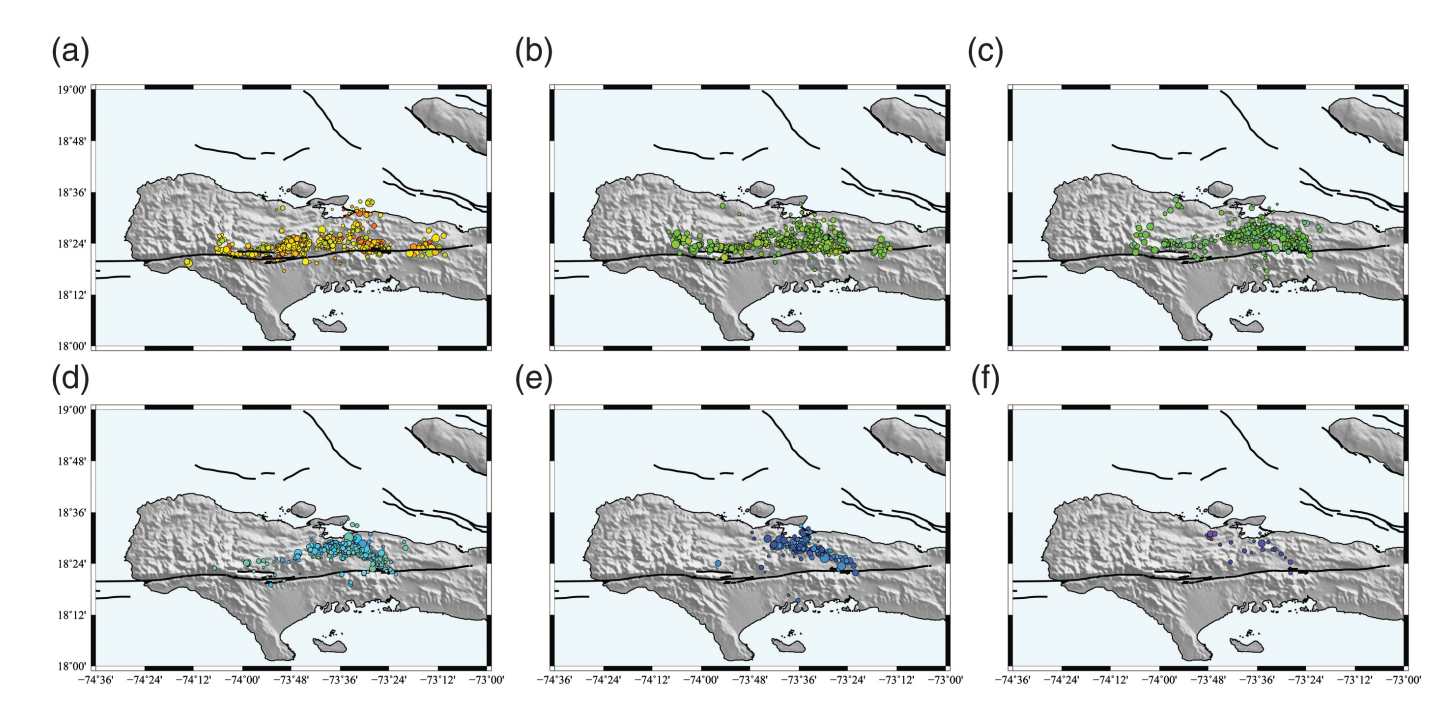
with a strike of N60°W  $\pm$  5°, N60°E  $\pm$  5°, and N85°E  $\pm$  5°, respectively.

For all the clusters, we observe very few near-surface events, that is, located in the upper 4 km. The shallowest events are primarily located in the western cluster near the intersection with the central one, which is consistent with the sharp transition in the InSAR data indicative of surface rupture along the Ravine du Sud fault (Calais et al., 2022; Maurer et al., 2022). Figure 7b-d shows the aftershock locations coded by hypocenter depth but for different time intervals. Although more than 50% of the events occurred between 20 August and 30 September, for the remaining days in the catalog, the aftershocks still display the same behaviors where the central and western cluster have significantly fewer events compared to the eastern one, whereas the deeper events are clustered in the eastern zone. We did not observe a clear migration of the aftershocks during either time slice; events were continuously occurring on all the clusters (Fig. 7 and Fig. S2). We also observe a small cluster of shallower aftershocks, less than 15 km long, outside of the mainshock area, and to the east (longitude -73.25°) with events that occurred primarily during the first month after the mainshock. They are likely related to

**Figure 7.** Aftershock locations from hypoDD color coded by hypocenter depth and sized with respect to their magnitudes. The black triangles show the local seismic station distribution. The top left is a map view of seismicity, the right and bottom panels are with respect to depth. (a) Complete catalog of 2520 events between the period of 20 August and 31 December 2021, (b) events between 20 August and 30 September of the catalog, (c) events between 1 October and 14 November of the catalog, and (d) events between 15 November and 31 December of the catalog.

shallow triggered afterslip along the EPG fault, as documented by Maurer *et al.* (2022) and H. Z. Yin *et al.* (unpublished manuscript, 2022, see Data and Resources).

The *P*-wave first-motion focal mechanism nodal planes match the overall pattern of the aftershock distribution (see Table S2 for a complete list of the focal mechanisms). Figure 9 shows the focal mechanisms sorted by the plunge of their principal axes (following Zoback, 1992), in which the red focal mechanisms indicate primarily thrust motion, the green ones strike-slip events, and the black ones are the rest. The events within the eastern cluster are primarily composed of thrust and left strike-slip motion consistently with the coseismic rupture models (Calais *et al.*, 2022; Maurer *et al.*, 2022; Okuwaki and



Fan, 2022). Most importantly, one of the nodal planes for most of these events is parallel to the northwest-southeast, as illustrated by the aftershocks. Furthermore, the western cluster is mostly composed of left-lateral strike-slip mechanisms with nodal planes that are aligned with the direction of the Ravine du Sud fault, consistent with the aftershock distribution. Nevertheless, a more detailed analysis of the focal mechanisms is necessary to confirm this assertion.

## **DISCUSSION**

# Was the EPG fault part of the main rupture?

The 2021  $M_{\rm w}$  7.2 Nippes, Haiti, earthquake can now be added to a long list of complex branch fault earthquakes involving rupture along multiple fault segments such as the 1979 Imperial Valley (Archuleta, 1984), the 1980 El Asnam (Cisternas et al., 1982; Yielding, 1985), the 1980 Irpinia (Bernard et al., 1993), the 1992 Landers earthquake (Sowers et al., 1994), the 1999 Hector mine earthquake (Treiman et al., 2002), the 2002 Denali earthquake (Frankel, 2004), the 2010 Darfield earthquake (Beavan et al., 2012), the 2010 El Mayor-Cucapah earthquake (Hauksson et al., 2011), the 2010 Haiti earthquake (Meng et al., 2012; Douilly et al., 2013; Symithe et al., 2013), and the 2016 Kaikoura earthquake (Xu et al., 2018). This event ruptured several north dipping segments close to the EPG fault in a pattern that is similar to the 2010 rupture further east (Douilly et al., 2013). It is important to note that the dip angle of the EPG fault is not directly constrained in the area of the 2021 rupture, though this fault is believed to be primarily vertical or southdipping near the 2010 mainshock (Prentice et al., 2010). However, one cannot rule out a variable dip along strike for the EPG fault in accordance with the spatial distribution of the topography. Near the 2010 rupture, the high topography is located to the south of the rupture, consistent with the south

**Figure 8.** Aftershock hypocenters at different depth intervals. (a) 4–8, (b) 8–12, (c) 12–16, (d) 16–20, (e) 20–24, and (f) 24–28 km.

dipping configuration of the EPG fault inferred by Prentice *et al.* (2010) further east. However, near the 2021 mainshock, the high topography is located to the north of the rupture (Pic Macaya) and, thus, without the presence of other north-dipping secondary faults; a north-dipping EPG fault could explain the high topography north of the surface trace. This warped fault configuration with laterally variable dip has also been inferred for the San Andreas fault (SAF) (Fuis *et al.*, 2012)—another plate boundary fault in a similar tectonic setting. Using potential

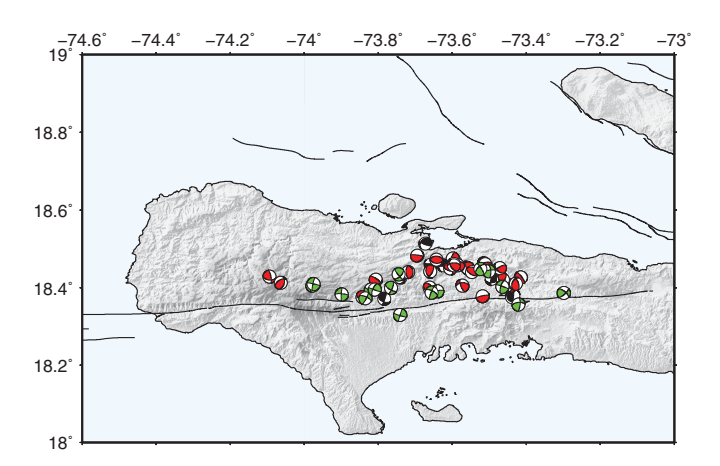


**Figure 9.** *P*-wave first-motion focal mechanisms for 53 events categorized by the plunge of their principal stresses based on the classification of Zoback (1992). Thrust mechanisms are represented in red, strike-slip mechanisms are in green, and the black mechanisms indicate the unclassified type of faulting.

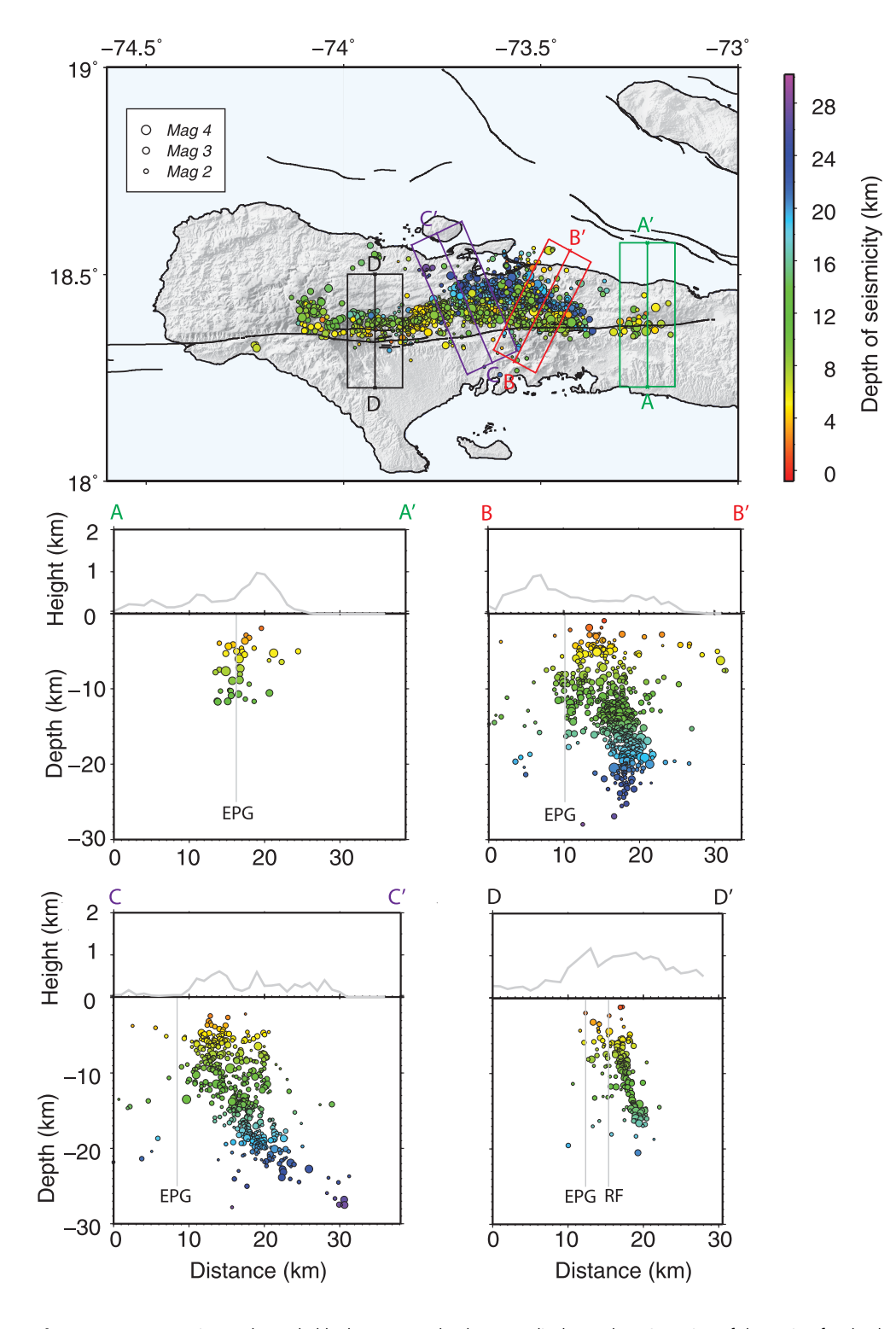


**Figure 10.** Cross sections color coded by hypocenter depth perpendicular to the orientation of the main aftershock clusters. Hypocenters included within a box are projected into the corresponding cross sections. Gray curve above each cross section indicates the surface topography. The vertical gray lines mark the location of either the Enriquillo Plantain Garden (EPG) fault or the Ravine du Sud fault (RF).

field data, active source imaging, and seismicity, Fuis et al. (2012) indicate that the SAF dips to the southwest north of the Big Bend area but immediately rotates to a northeast dip after the bend, consistent with the asymmetric topography in

that region. However, considering the lack of evidence for a dipping EPG fault in our study area, in the following, we will assume the EPG fault to be purely vertical.

Considering the proximity of those ruptured segments to the nearby EPG fault, it is worth investigating whether the latter did participate in this earthquake, as the outcome could alter seismic hazard estimates for this region following the 2021 rupture. Therefore, to further understand the geometry of the structures and investigate the likelihood for the main structures to coincide with the EPG fault, we displace in Figure 10a series of cross sections perpendicular to the orientation of each aftershock cluster. Events in cross section A-A' located outside of the rupture zone delineate a vertical structure that is in agreement with the assumption of a vertical EPG fault. These events coincide with the zone of afterslip that has been observed using InSAR data (Maurer et al., 2022; H. Z. Yin et al., unpublished manuscript, 2022, see Data and Resources). In cross section B-B,' which is perpendicular to the northwest-southeaststriking direction of the eastern cluster, we observe that the aftershocks delineate primarily north-dipping segment  $(\sim60^{\circ}-65^{\circ})$ , though its dip angle seems to be steeper below 18 km depth. Moreover, we find aftershocks along the vertical projection of the EPG surface fault trace (vertical gray line in Fig. 10) near 10 km

depth. This suggests that the eastern cluster occurred on a fault north of, and separate from, the EPG fault—a pattern similar to with the Léogâne fault rupture during the 2010 earthquake (Calais *et al.*, 2010; Mercier de Lépinay *et al.*, 2011; Symithe

et al., 2013). Aftershocks within the central cluster in cross section C–C′ define a dip angle down to 18 km that is consistent with the eastern cluster but appear to dip at a slightly shallower angle below that depth. Finally, aftershocks in cross section D–D′ show a clear ~N75° dip angle on a fault segment that coincides with the Ravine du sud fault, parallel to the EPG fault but separate from it, in accordance with slip inversion from InSAR data (Calais et al., 2022; Maurer et al., 2022).

We also display north-south, northeast-southwest, and northwest-southeast directed cross sections in Figure 11, Figures S1 and S2. Cross section A-A' in Figure 11 and Figure S2 clearly shows events on the EPG fault (assumed to be vertical) that may have been triggered by the mainshock. Events within cross sections B-B' and C-C' show a north-dipping structure adjacent to the EPG fault. We observe a rotation in strike between the eastern and central clusters in cross section E-E' in Figure 11 and Figure S2. Overall, our favored interpretation of the 2021 Nippes earthquake involves the rupture of north-dipping faults separate from the main EPG fault, with a compressional bend configuration.

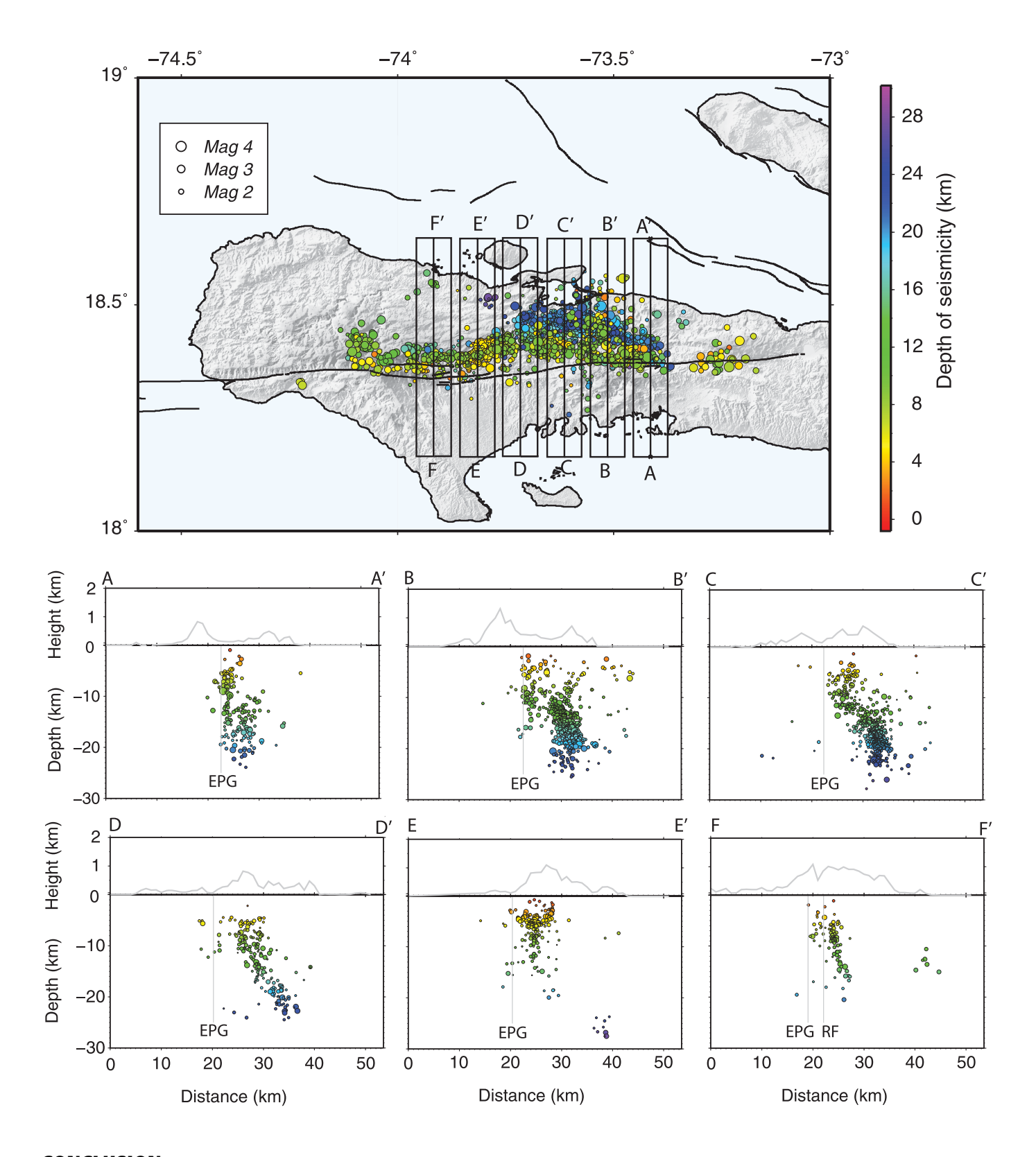
This raises the question as to why would the rupture favor secondary, compressional faults rather than the perhaps more mature EPG fault? This was observed during the 1989 Loma Prieta earthquake in California, where the rupture occurred on a steeply dipping thrust fault near the main SAF (Dietz and Ellsworth, 1990). This was also the case for the 2010 Haiti earthquake, in which Douilly et al. (2015) argued that the geometry of the faults and, particularly, a weak (lower friction) eastern Léogâne fault were necessary for the rupture to break both north-dipping segments and bypass the EPG fault. We hypothesize that this could also be the case for the 2021 rupture. In addition, the fact that the EPG fault did not rupture does not imply that the 2021 rupture had no impact on that fault. In the case of the 2010 Haiti earthquake, the Léogâne fault rupture intersected the EPG fault at depth, causing an increase in stresses in the upper part of the EPG fault and a decrease below the intersection (Symithe et al., 2013; Douilly et al., 2015). Given the similarity in rupture pattern between the 2010 and 2021 events, and the fact that the surface projection of the ruptured segments intersect the EPG fault near the surface and not at depth, one would expect the 2021 rupture to cause a slight decrease in shear stress on the EPG fault segments adjacent to the ruptured structures. Future Coulomb stress change calculations on nearby faults, and dynamic rupture studies are needed to clarify this hypothesis about the shear stress variation on the EPG fault.

### Activation of secondary faults

Following major crustal earthquakes, aftershocks can sometimes occur on secondary structures (Hauksson *et al.*, 1993; Shearer *et al.*, 2003; Douilly *et al.*, 2013; Shelly, 2020), that is, fault segments that did not slip coseismically during the mainshock but were activated or triggered due to mechanisms

such as creep, postseismic deformation, static or dynamic stress change, and so forth. Such secondary faults were observed following the 2019 Ridgecrest sequence. This earthquake involved two main events of magnitudes 6.4 and 7.1 with complex rupture on nearly parallel and nearly perpendicular fault segments (DuRoss et al., 2020; Ponti et al., 2020; Shelly, 2020). The  $M_{\rm w}$  6.4 event occurred on a set of left-lateral faults and the  $M_{\rm w}$  7.1 one took place nearly 36 hr later on a right-lateral fault that crossed the left-lateral fault system. This event triggered significant seismicity on the Garlock fault, particularly on the segment close to the rupture area (Shelly, 2020) where shallow creep and shear stress increase have been observed (Ramos et al., 2020; Toda and Stein, 2020). Furthermore, the aftershock distribution delineated numerous cross-cutting faults perpendicular to the right-lateral fault (Shelly, 2020). The activation of these secondary cross-cutting structures was also corroborated by phase gradient analysis with InSAR, where those surface fractures showed slip polarity in retrograde with the background tectonic stress (Xu et al., 2020). Secondary structures were also observed during the 2010 Haiti earthquake. The offshore Trois Baies fault experienced significant seismicity following the mainshock (Douilly et al., 2013), consistent with coseismic Coulomb stress change calculations (Symithe et al., 2013). In addition, the aftershocks also delineated antithetic and cross-cutting structures with respect to the fault segments that ruptured during the main event (Douilly et al., 2013).

Consistent with those crustal earthquakes, the aftershock sequence that followed the 2021 Nippes earthquake activated several secondary structures. Similar to the 2010 earthquake, the 2021 rupture also triggered significant seismicity along offshore faults (see ayiti-séismes); though we did not incorporate these events in this analysis as their locations are not well constrained, because they occurred outside of the footprint of our network. In addition, the aftershocks seem to delineate some north-south-striking secondary structures. In map view, these structures are for the most part buried within the central cluster of seismicity. But if we analyze the catalog between November and December (Fig. 7d), the aftershocks show alignments different from the orientation of the central cluster described earlier. Although the presence of these structures in map view is debatable, there are some focal mechanisms within that region that have one of their nodal planes parallel to the orientation of these secondary structures, which further support this hypothesis (Fig. 8). These structures can also be seen in cross sections B-B' and C-C' in Figure S3 and C-C' in Figure 10 where the aftershocks delineate some south-dipping fault planes. Moreover, phase gradient analysis of InSAR images (Sandwell and Price, 1998; Sandwell et al., 2000; Xu et al., 2020), applied to the 2021 Nippes earthquake, revealed the presence of some secondary fault features (H. Z. Yin et al., unpublished manuscript, 2022, see Data and Resources) in agreement with our interpretation.



# **CONCLUSION**

In this study, we used data from a local seismic station deployment from 20 August to 31 December 2021 to perform a high-resolution aftershock relocation for the 2021  $M_{\rm w}$  7.2 Nippes earthquake in southern Haiti. We find two small clusters of events located on the EPG fault. The first one is located just to the east of the rupture area, coincident with afterslip observed in InSAR data.

**Figure 11.** North—south cross sections illustrating the correlation of the fault structures with respect to the EPG fault. Hypocenters within the rectangular box are projected into the corresponding cross sections. Gray curve above each cross section indicates the surface topography. The vertical gray lines mark the location of either the EPG fault or the RF fault.

The second one is located in the near vicinity of the hypocenter, in which some events delineate a vertical structure that coincides with the vertical projection of the surface trace of the EPG fault. However, the majority of the seismicity is located on structures that are adjacent to the EPG fault, which indicates that the EPG fault proper likely did not rupture during the Nippes earthquake and remains a source of significant regional hazard.

The majority of the aftershocks form three separate clusters with slightly different strike and dip. The eastern one defines a fault segment north of the EPG fault with a strike of N60°W  $\pm$  5° and a dip of  $\sim 60^{\circ}$  toward the north. The central one has a similar dip as the eastern one, but the strike rotates to ~N60°E. The western one follows the surface trace of the Ravine du Sud fault, with an east-west strike and northward dip of about ~75°. The spatial distribution of aftershocks is not uniform, as the eastern cluster has significantly more events compared to the central and western ones, with deeper events in the eastern cluster as well (greater than 18 km depth). We did not investigate the Moho depth in this study. Variable Moho depth was observed on a north-south configuration near the capital Port-au-Prince from receiver function analysis where the Moho was imaged at 22 km in the south and increased to 41 km in central Haiti (Corbeau et al., 2017). Future receiver function studies should be considered to investigate whether the Moho depth is also variable throughout the Southern Peninsula.

We also invert for a 1D P and S velocity structure for this region. In general, the final P and S velocities for almost all the layers are consistently smaller compared to the velocities near the 2010 Haiti mainshock. This suggests the presence of lateral velocity heterogeneity near the 2021 mainshock area. Prominent low- and fast-velocity anomalies were observed near the 2010 ruptured area, and bimaterial interfaces were observed along all the fault segments (Douilly et al., 2016). Bimaterial interfaces can sometimes generate dynamic dilatation at one end of a rupture and dynamic compression at the other end, which could cause the rupture to die in the direction of compression and facilitate the rupture to propagate in the dilational direction (Shi and Ben-Zion, 2006). Therefore bimaterial interfaces along the EPG fault and the 2021 ruptured segments could potentially explain the unilateral nature of this event where the rupture only propagates west of the hypocenter. Local earthquake tomography and ambient noise tomography with the existing data should be considered in the future to not only define a 3D crustal structure for this region but also to investigate the likelihood of bimaterial interfaces.

## **DATA AND RESOURCES**

The seismic data were collected by a temporary broadband stations following the 2021 Nippes earthquake in Haiti and will be available through the Incorporated Research Institutions for Seismology (IRIS) Data Center. Additional data from RS stations are obtained from the webservice International Federation of Digital Seismograph Networks (FDSN) of the Ayiti-seismes platform (https://ayiti.unice.fr/ayiti-seismes/fdsnws/, last accessed March 2022) and the IRIS Data Center. The stations used in

this study are composed of four RS of the HY Haiti network (doi: 10.7914/SN/HY) and 12 broadband stations of the Z2 Haiti network (doi: 10.7914/SN/Z2\_2021). SeisComp3 (SC3, https://www.seiscomp. de/, last accessed February 2022) is used for the real-time monitoring of the seismic data. The figures in this study are plotted with Generic Mapping Tools (GMT; Wessel and Smith, 1998; Wessel et al., 2019). This article includes the supplemental material that consists of (1) Figure S1 showing cross sections with respect to time perpendicular to the orientation of the main aftershock clusters, (2) Figure S2 showing northeast-southwest cross sections illustrating possible fault structures, (3) Figure S3 showing northwest-southeast cross sections illustrating possible fault structures, (4) Table S1 with the Final hypoDD catalog for the 2520 events shown in Figures 7, 8, 10, and 11, and (5) Table S2 with the P-wave first-motion focal mechanisms for the 53 events used in this study. The unpublished manuscripts cited in the text are by E. Calais, S. J. Symithe, and B. M. de Lépinay (2022), "Strain partitioning within the Caribbean-North America transform plate boundary in southern Haiti, tectonic and hazard implications", submitted to Bull. Seismol. Soc. Am. and H. Z. Yin, X. Xu, J. Haase, R. Douilly, D. T. Sandwell, and B. de Lépinay (2022), "Surface deformation surrounding the 2021 M7.2 Haiti earthquake illuminated by InSAR observations,' Bull. Seismol. Soc. Am.

## **DECLARATION OF COMPETING INTERESTS**

The authors declare that there are no conflicts of interest recorded.

## **ACKNOWLEDGMENTS**

This project received support from several institutions and projects. The authors thank Susan Hough and an anonymous reviewer for their helpful comments that helped improved the article. This research was supported by Grants from the U.S. National Science Foundation (Award Number EAR-2217976 to Roby Douilly). Startup fund to Roby Douilly was used to ship the Nanometric broadband stations to Haiti. Funding to Eric Calais was provided by the FEDER European Community program within the Interreg Caraïbes "PREST" project. Eric Calais acknowledges support from the Institut Universitaire de France and from the French National Research Agency (Project Number ANR-21CE03-0010 "OSMOSE"). This project has been supported via Steeve J. Symithe by the Grant and Cooperative Agreement between U.S. Geological Survey (USGS) (G20AC00100) and the Faculté Des Sciences (FDS) of the State University of Haiti (UEH). Funding from this grant was provided by the USAID Bureau of Humanitarian Assistance. Steeve J. Symithe also acknowledges that funds from the "Fonds D'appui à la Recherche" (FAR) of the Rectorat of States University of Haiti (RUEH) have been used to support partly deployment of broadband stations within the epicentral area of the 2021 Nippes earthquake a few days after the mainshock. Sylvert Paul is supported by a grant from the French Embassy in Haiti and funding from the Université Côte d'Azur, France. The authors acknowledge the Institut de Recherche pour le Développement (IRD) and the Université d'Etat d'Haïti (UEH) who provided financial support, human resources, and logistical means for the installation and maintenance of the temporary field stations. Some of the Raspberry Shake (RS) instruments were acquired as part of the Interreg Caribbean project "PREST" of the FEDER European Community program and the CNRS-IRD project "S2RHAI". The Bureau of Mines and Energy (BME) of Haiti

helped with the transportation as their contribution to the deployment of the broadband stations. The authors are grateful to the citizen-hosts of the RS stations who made it possible to monitor seismic activity in real time from the mainshock of the Nippes earthquake on 14 August-31 December 2021—the end date of this study. The authors would also thank all the people who, in one way or another, allowed the installation of the temporary seismological stations in the epicentral zone and ensured the security of these stations throughout the experiment, despite a complicated social, political, economic, and climatic context.

#### **REFERENCES**

- Allen, R. (1982). Automatic phase pickers: Their present use and future prospects, Bull. Seismol. Soc. Am. 72, no. 6B, S225-S242.
- Anthony, R. E., A. T. Ringler, D. C. Wilson, and E. Wolin (2019). Do low-cost seismographs perform well enough for your network? An overview of laboratory tests and field observations of the OSOP Raspberry Shake 4D, Seismol. Res. Lett. 90, no. 1, 219-228.
- Archuleta, R. J. (1984). A faulting model for the 1979 Imperial Valley earthquake, J. Geophys. Res. 89, no. B6, 4559-4585.
- Bakun, W. H., C. H. Flores, and U. S. ten Brink (2012). Significant earthquakes on the Enriquillo fault system, Hispaniola, 1500-2010: Implications for seismic hazard, Bull. Seismol. Soc. Am. 102, no. 1, 18-30.
- Beavan, J., M. Motagh, E. J. Fielding, N. Donnelly, and D. Collett (2012). Fault slip models of the 2010-2011 Canterbury, New Zealand, earthquakes from geodetic data and observations of postseismic ground deformation, New Zeal. J. Geol. Geophys. 55, no. 3, 207-221.
- Benford, B., C. DeMets, and E. Calais (2012). GPS estimates of microplate motions, northern Caribbean: Evidence for a Hispaniola microplate and implications for earthquake hazard, Geophys. J. Int. 191, no. 2, 481-490.
- Bernard, P., A. Zollo, C.-I. Trifu, and A. Herrero (1993). Details of the rupture Kinematics and mechanism of the 1980 Irpinai earthquake: New results and remaining questions, Ann. Geophy. 36, no. 1, 71–80.
- Calais, E., A. Freed, G. Mattioli, F. Amelung, S. Jónsson, P. Jansma, S.-H. Hong, T. Dixon, C. Prépetit, and R. Momplaisir (2010). Transpressional rupture of an unmapped fault during the 2010 Haiti earthquake, Nature Geosci. 3, no. 11, 794-799.
- Calais, E., S. Symithe, T. Monfret, B. Delouis, A. Lomax, F. Courboulex, J. P. Ampuero, P. Lara, Q. Bletery, J. Chèze, et al. (2022). Citizen seismology helps decipher the 2021 Haiti earthquake, Science 376, no. 6590, 283-287.
- Cisternas, A., J. Dorel, and R. Gaulon (1982). Models of the complex source of the El Asnam earthquake, Bull. Seismol. Soc. Am. 72, no. 6A, 2245-2266.
- Corbeau, J., F. Rolandone, S. Leroy, K. Guerrier, D. Keir, G. Stuart, V. Clouard, R. Gallacher, S. Ulysse, D. Boisson, et al. (2017). Crustal structure of western Hispaniola (Haiti) from a teleseismic receiver function study, Tectonophysics 709, 9-19.
- Dietz, L. D., and W. L. Ellsworth (1990). The October 17, 1989, Loma Prieta, California, earthquake and its aftershocks: Geometry of the sequence from high-resolution locations, Geophys. Res. Lett. 17, no. 9, 1417-1420.
- Douilly, R., H. Aochi, E. Calais, and A. Freed (2015). Three-dimensional dynamic rupture simulations across interacting faults: The Mw7. 0, 2010, Haiti earthquake, J. Geophys. Res. 120, no. 2, 1108-1128.
- Douilly, R., W. L. Ellsworth, E. Kissling, A. M. Freed, A. Deschamps, and B. LépinayMercier de (2016). 3-D velocity structure in

- southern Haiti from local earthquake tomography, J. Geophys. Res. 121, no. 12, 8813-8832.
- Douilly, R., J. S. Haase, W. L. Ellsworth, M.-P. Bouin, E. Calais, S. J. Symithe, J. G. Armbruster, B. M. de Lépinay, A. Deschamps, S.-L. Mildor, et al. (2013). Crustal structure and fault geometry of the 2010 Haiti earthquake from temporary seismometer deployments, Bull. Seismol. Soc. Am. 103, no. 4, 2305-2325.
- DuRoss, C. B., R. D. Gold, T. E. Dawson, K. M. Scharer, K. J. Kendrick, S. O. Akciz, S. J. Angster, J. Bachhuber, S. Bacon, S. E. Bennett, et al. (2020). Surface displacement distributions for the July 2019 Ridgecrest, California, earthquake ruptures, Bull. Seismol. Soc. Am. 110, no. 4, 1400-1418.
- Ester, M., H.-P. Kriegel, J. Sander, and X. Xu (1996). A density-based algorithm for discovering clusters in large spatial databases with noise, KDD'96: Proc. of the Second International Conference on Knowledge Discovery and Data Mining, no. 34, 226-231.
- Frankel, A. (2004). Rupture process of the M 7.9 Denali fault, Alaska, earthquake: Subevents, directivity, and scaling of high-frequency ground motions, Bull. Seismol. Soc. Am. 94, no. 6B, S234-S255.
- Fuis, G. S., D. S. Scheirer, V. E. Langenheim, and M. D. Kohler (2012). A new perspective on the geometry of the San Andreas fault in southern California and its relationship to lithospheric structure, Bull. Seismol. Soc. Am. 102, no. 1, 236-251.
- Hardebeck, J., and P. Shearer (2008). HASH: A FORTRAN program for computing earthquake, First-Motion Focal Mechanisms-v1. 2, U.S. Geol. Surv. Institution of Oceanography, 1-17.
- Hauksson, E., L. M. Jones, K. Hutton, and D. Eberhart-Phillips (1993). The 1992 Landers earthquake sequence: Seismological observations, J. Geophys. Res. 98, no. B11, 19,835-19,858.
- Hauksson, E., J. Stock, K. Hutton, W. Yang, J. A. Vidal-Villegas, and H. Kanamori (2011). The 2010 Mw 7.2 El Mayor-Cucapah earthquake sequence, Baja California, Mexico and southernmost California, USA: Active seismotectonics along the Mexican Pacific Margin, Pure Appl. Geophys. 168, nos. 8/9, 1255-1277.
- Hayes, G., R. Briggs, A. Sladen, E. Fielding, C. Prentice, K. Hudnut, P. Mann, F. Taylor, A. Crone, R. Gold, et al. (2010). Complex rupture during the 12 January 2010 Haiti earthquake, Nature Geosci. 3, no. 11, 800-805.
- Kissling, E., W. Ellsworth, D. Eberhart-Phillips, and U. Kradolfer (1994). Initial reference models in local earthquake tomography, J. Geophys. Res. 99, no. B10, 19,635-19,646.
- Kissling, E., U. Kradolfer, and H. Maurer (1995). Program VELEST USERS GUIDE-Short Introduction, Institute of Geophysics, ETH Zurich.
- Maeda, N. (1985). A method for reading and checking phase times in autoprocessing system of seismic wave data, Zisin 38, 365-379.
- Mann, P., F. Taylor, R. L. Edwards, and T.-L. Ku (1995). Actively evolving microplate formation by oblique collision and sideways motion along strike-slip faults: An example from the northeastern Caribbean plate margin, Tectonophysics 246, nos. 1/3, 1-69.
- Maurer, J., R. Dutta, A. Vernon, and S. Vajedian (2022). Complex rupture and triggered aseismic creep during the August 14, 2021 Haiti earthquake from satellite geodesy, Geophys. Res. Lett. 49, no. 11, e2022GL098573, doi: 10.1029/2022GL098573.
- Meng, L., J.-P. Ampuero, A. Sladen, and H. Rendon (2012). High-resolution backprojection at regional distance: Application to the Haiti M7. 0 earthquake and comparisons with finite source studies, J. Geophys. Res. 117, no. B4, doi: 10.1029/2011JB008702.

- Mercier de Lépinay, B., A. Deschamps, F. Klingelhoefer, Y. Mazabraud, B. Delouis, V. Clouard, Y. Hello, J. Crozon, B. Marcaillou, D. Graindorge, et al. (2011). The 2010 Haiti earthquake: A complex fault pattern constrained by seismologic and tectonic observations, Geophys. Res. Lett. 38, no. 22, doi: 10.1029/2011GL049799.
- Nettles, M., and V. Hjörleifsdóttir (2010). Earthquake source parameters for the 2010 January Haiti mainshock and aftershock sequence, *Geophys. J. Int.* **183**, no. 1, 375–380.
- Okuwaki, R., and W. Fan (2022). Oblique convergence causes both thrust and strike-slip Ruptures during the 2021 M 7.2 Haiti earth-quake, *Geophys. Res. Lett.* **49**, no. 2, e2021GL096373, doi: 10.1029/2021GL096373.
- Ponti, D. J., J. L. Blair, C. M. Rosa, K. Thomas, A. J. Pickering, S. Akciz, S. Angster, J.-P. Avouac, J. Bachhuber, S. Bacon, et al. (2020). Documentation of surface fault Rupture and ground-deformation features produced by the 4 and 5 July 2019 Mw 6.4 and Mw 7.1 Ridgecrest earthquake sequence, Seismol. Res. Lett. 91, no. 5, 2942–2959.
- Possee, D., D. Keir, N. Harmon, C. Rychert, F. Rolandone, S. Leroy, J. Corbeau, G. Stuart, E. Calais, F. Illsley-Kemp, et al. (2019). The tectonics and active faulting of Haiti from seismicity and tomography, *Tectonics* 38, no. 3, 1138–1155.
- Prentice, C., P. Mann, A. Crone, R. Gold, K. Hudnut, R. Briggs, R. Koehler, and P. Jean (2010). Seismic hazard of the Enriquillo-Plantain Garden fault in Haiti inferred from paleoseismology, *Nature Geosci.* **3**, no. 11, 789–793.
- Quiros, D. A., J. Pulliam, D. Barman, E. Polanco Rivera, and V. Huerfano (2018). Ambient noise tomography images accreted terranes and igneous provinces in Hispaniola and Puerto Rico, Geophys. Res. Lett. 45, no. 22, 12–293.
- Ramos, M. D., J. C. Neo, P. Thakur, Y. Huang, and S. Wei (2020). Stress changes on the Garlock fault during and after the 2019 Ridgecrest earthquake sequence, *Bull. Seismol. Soc. Am.* **110**, no. 4, 1752–1764.
- Ratchkovski, N. A., S. Wiemer, and R. A. Hansen (2004). Seismotectonics of the central Denali fault, Alaska, and the 2002 Denali fault earthquake sequence, *Bull. Seismol. Soc. Am.* **94**, no. 6B, S156–S174.
- Saint Fleur, N., N. Feuillet, R. Grandin, E. Jacques, J. Weil-Accardo, and Y. Klinger (2015). Seismotectonics of southern Haiti: A new faulting model for the 12 January 2010 M7. 0 earthquake, *Geophys. Res. Lett.* **42**, no. 23, 10–273.
- Saint Fleur, N., Y. Klinger, and N. Feuillet (2020). Detailed map, displacement, paleoseismology, and segmentation of the Enriquillo-Plantain Garden Fault in Haiti, *Tectonophysics* 778, 228368, doi: 10.1016/j.tecto.2020.228368.
- Sandwell, D. T., and E. J. Price (1998). Phase gradient approach to stacking interferograms, *J. Geophys. Res.* **103**, no. B12, 30,183–30,204.
- Sandwell, D. T., L. Sichoix, D. Agnew, Y. Bock, and J.-B. Minster (2000).
  Near real-time radar interferometry of the Mw 7.1 Hector Mine earthquake, *Geophys. Res. Lett.* 27, no. 19, 3101–3104.
- Scherer, J. (1912). Great earthquakes in the island of Haiti, Bull. Seismol. Soc. Am. 2, no. 3, 161-180.
- Shearer, P. M., J. L. Hardebeck, L. Astiz, and K. B. Richards-Dinger (2003). Analysis of similar event clusters in aftershocks of the 1994 Northridge, California, earthquake, J. Geophys. Res. 108, no. B1, doi: 10.1029/2001JB000685.
- Shelly, D. R. (2020). A high-resolution seismic catalog for the initial 2019 Ridgecrest earthquake sequence: Foreshocks, aftershocks, and faulting complexity, *Seismol. Res. Lett.* **91**, no. 4, 1971–1978.

- Shi, Z., and Y. Ben-Zion (2006). Dynamic rupture on a bimaterial interface governed by slip-weakening friction, *Geophys. J. Int.* **165**, no. 2, 469–484.
- Sowers, J., J. Unruh, W. Lettis, and T. Rubin (1994). Relationship of the Kickapoo fault to the Johnson Valley and Homestead Valley faults, San Bernardino County, California, *Bull. Seismol. Soc. Am.* 84, no. 3, 528–536.
- Symithe, S., E. Calais, J. Chabalier, R. Robertson, and M. Higgins (2015). Current block motions and strain accumulation on active faults in the Caribbean, *J. Geophys. Res.* **120**, no. 5, 3748–3774.
- Symithe, S. J., E. Calais, J. S. Haase, A. M. Freed, and R. Douilly (2013). Coseismic slip distribution of the 2010 M 7.0 Haiti earthquake and resulting stress changes on regional faults, *Bull. Seismol. Soc. Am.* **103**, no. 4, 2326–2343.
- Toda, S., and R. S. Stein (2020). Long-and short-term stress interaction of the 2019 Ridgecrest sequence and coulomb-based earthquake forecasts, *Bull. Seismol. Soc. Am.* 110, no. 4, 1765– 1780.
- Treiman, J. A., K. J. Kendrick, W. A. Bryant, T. K. Rockwell, and S. F. McGill (2002). Primary surface rupture associated with the Mw 7.1
  16 October 1999 Hector Mine earthquake, San Bernardino County, California, Bull. Seismol. Soc. Am. 92, no. 4, 1171–1191.
- Vogt, J. (2004). A glimpse at the historical seismology of the West Indies, *Ann. Geophys* **47**, no. 2, 465–476.
- Vogt, J. (2005). Deux séismes majeurs de Sainte-Domingue au XVIIIéme siécle. 2. Le séisme du 3 juin 1770, *Genéalogie Det Histoire de La Caraïbe* 178, 4424–4432 (in French).
- Waldhauser, F. (2001). HypoDD–A program to compute double-difference hypocenter locations, *U.S. Geol. Surv. Open-File Rept.* 2001-113, doi: 10.3133/ofr01113.
- Waldhauser, F., and W. L. Ellsworth (2000). A double-difference earth-quake location algorithm: Method and application to the northern Hayward fault, California, Bull. Seismol. Soc. Am. 90, no. 6, 1353–1368.
- Waldhauser, F., and W. L. Ellsworth (2002). Fault structure and mechanics of the Hayward fault, California, from double-difference earthquake locations, *J. Geophys. Res.* **107**, no. B3, ESE 3-1–ESE 3-15.
- Wessel, P., and W. H. Smith (1998). New, improved version of generic mapping tools released, *Eos Trans. AGU* **79**, no. 47, 579.
- Wessel, P., J. F. Luis, L. Uieda, R. Scharroo, F. Wobbe, W. H. F. Smith, and D. Tian (2019). The generic mapping tools version 6, geochemistry, *Geophys. Geosystems* **20**, no. 11, 5556–5564, doi: 10.1029/2019GC008515.
- Xu, W., G. Feng, L. Meng, A. Zhang, J. P. Ampuero, R. Bürgmann, and L. Fang (2018). Transpressional rupture cascade of the 2016 Mw 7.8 Kaikoura earthquake, New Zealand, *J. Geophys. Res.* **123**, no. 3, 2396–2409.
- Xu, X., D. T. Sandwell, and B. Smith-Konter (2020). Coseismic displacements and surface fractures from Sentinel-1 InSAR: 2019 Ridgecrest earthquakes, Seismol. Res. Lett. 91, no. 4, 1979–1985.
- Yielding, G. (1985). Control of rupture by fault geometry during the 1980 El Asnam (Algeria) earthquake, *Geophys. J. Int.* **81**, no. 3, 641–670.
- Zoback, M. L. (1992). First-and second-order patterns of stress in the lithosphere: The World Stress Map Project, *J. Geophys. Res.* **97**, no. B8, 11,703–11,728.

Manuscript received 30 June 2022 Published online 13 October 2022